2012

# Role of Iron and Organic Carbon in Mass-specific Light Absorption by Particulate Matter from Louisiana Coastal Waters

Meg Estapa
*Skidmore College*

Emmanuel E. Boss

Mayer M. Lawrence

Roesler S. Collin



## Recommended Citation

Estapa, M.L., Boss E., Mayer L.M., Roesler C.R., 2012. Role of iron and organic carbon in mass-specific light absorption by particulate matter from Louisiana coastal waters, Limnology and Oceanography, 57(1): 97-112.

*Limnol. Oceanogr.*, 57(1), 2012, 97–112

doi:10.4319/lo.2012.57.1.0097

# Role of iron and organic carbon in mass-specific light absorption by particulate matter from Louisiana coastal waters

Margaret L. Estapa,[a,b,1,*] Emmanuel Boss,[a] Lawrence M. Mayer,[b] and Collin S. Roesler[c]

[a] School of Marine Sciences, University of Maine, Orono, Maine
[b] School of Marine Sciences, University of Maine, Darling Marine Center, Walpole, Maine
[c] Department of Earth and Oceanographic Sciences, Bowdoin College, Brunswick, Maine

*Abstract*

We investigated the influences of organic content and mineralogical composition on light absorption by mostly mineral suspended particles in aquatic and coastal marine systems. Mass-specific absorption spectra of suspended particles and surface sediments from coastal Louisiana and the lower Mississippi and Atchafalaya rivers were measured with a centered sample-mount integrating sphere and analyzed in conjunction with organic carbon (OC), hydrochloric acid– (HCl-) extractable iron, and dithionite-extractable iron contents. Compositions and absorption properties were comparable to published values for similar particles. Dithionite-extractable iron was strongly correlated with absorption at ultraviolet (UV) and blue wavelengths, while OC and HCl-extractable iron were weakly but positively correlated. Oxidative removal of OC from sediments caused small and variable changes in absorption, while dithionite extraction of iron oxides strongly reduced absorption. Shoulders in the absorption spectra corresponded to absorption bands of iron oxide minerals, and their intensities were well correlated to dithionite-extractable iron contents of the samples. These findings support a primary role for iron oxide and hydroxide minerals in the mass-specific absorption of mostly inorganic particles from the terrestrially influenced coast of Louisiana. Riverine particles had higher dithionite-extractable iron contents and iron oxide–specific absorption features than did marine particles, consistent with current knowledge regarding differential transport of particulate iron oxides and hydroxides through estuarine salinity gradients and reductive alteration of these oxide phases on the Louisiana shelf. The quantifiable dependence of UV absorption features on iron oxide content suggests that, under certain conditions, in situ hyperspectral absorption measurements could be designed to monitor water-column iron mineral transport and transformation.

Light-dependent biogeochemical processes and ocean color in surface waters of the coastal ocean partially depend on ultraviolet (UV) and visible light absorption by non-phytoplanktonic, suspended particles. In shallow or river-dominated coastal regions and estuaries, high concentrations of suspended inorganic particles limit light absorption by phytoplankton and, thus, primary production. Organic carbon (OC) associated with suspended particles can photochemically degrade to produce dissolved organic carbon (DOC) and dissolved inorganic carbon (DIC), as well as to release dissolved nutrients to the water column (Estapa and Mayer 2010; Southwell et al. 2010). Inorganic suspended particles also complicate optical proxy measurements of biogeochemical parameters—for instance, concentrations of particulate organic carbon (POC) via beam attenuation or scattering (Son et al. 2009; Woźniak et al. 2010) or colored dissolved organic matter (CDOM) concentration from satellite ocean color measurements (Bélanger et al. 2008).

Autochthonous cellular debris and other organic matter originating from cells have been implicated as the primary contributors to open-ocean absorption by detrital particles ($a_d$), which is determined after extraction of methanol-soluble pigments (Bricaud and Stramski 1990; Nelson and Robertson 1993). In the coastal ocean, an additional, sizable fraction of total particle absorption ($a_p$) also arises from organic and inorganic particles of terrestrial origin. By examining relative mass fractions of organic and inorganic particulate matter (Bowers and Binding 2006) or POC : mass ratios of suspended particles (Woźniak et al. 2010), several groups have determined sizable mineral contributions to $a_p$ in the coastal ocean.

Absorption spectra of primarily inorganic, coastal particles often show weak features that are qualitatively similar to absorption spectra of iron oxide minerals (Babin et al. 2003; Babin and Stramski 2004). Two studies to date relate particulate iron content to the mass-specific absorption of particles ($a_p^*(\lambda)$) in marine or aquatic systems, but in both, the method of iron determination was relatively nonspecific, detecting many forms of mineral iron, some perhaps more absorbing than others. Babin and Stramski (2004) related ultrasonication-assisted, hydrochloric acid–(HCl-) extractable iron content to $a_p^*(\lambda)$ in terrestrial dust samples, but the correlation was dominated by a handful of samples with very high iron contents ($> 15\%$ by weight). Effler et al. (2011) showed a correlation between $a_p^*(400)$ and iron-specific X-ray intensity from aquatic particles using scanning electron microscopy, but two medium-intensity samples dominated the relationship, and inclusion of the two highest-intensity samples weakened it. Here, we test the idea that a specific subpool of mineral iron, composed of the easily reducible oxides and amorphous forms, is responsible for much of the mineral-specific absorption in suspended marine and aquatic particles.

* Corresponding author: mestapa@whoi.edu

[1] Present address: Marine Chemistry and Geochemistry, Woods Hole Oceanographic Institution, Woods Hole, Massachusetts

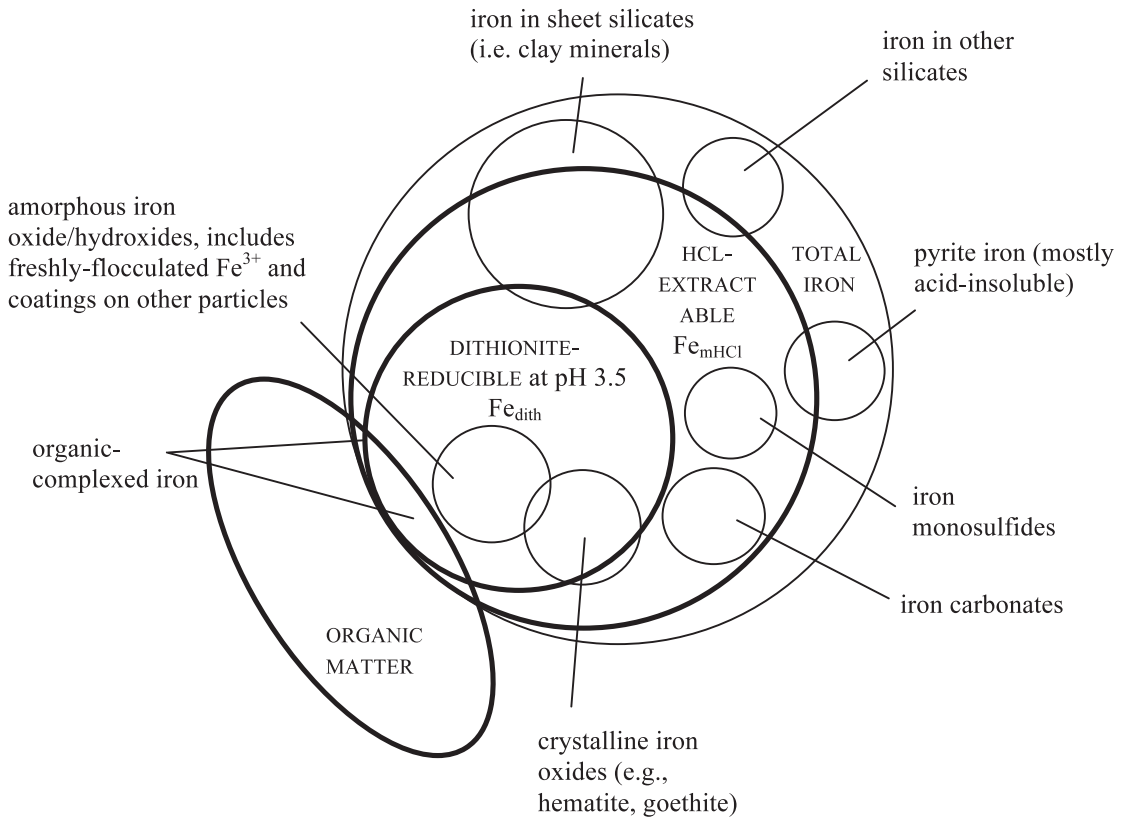


Fig. 1. Diagram showing probable relationships among the analytical windows of extraction methods in this study, and the iron phases that were likely present in particle samples. Circles and ellipses with heavy lines denote fractions targeted under specific analytical conditions used here. Relative sizes and overlapping areas of circles and ellipses are unrelated to actual concentrations of subpools. Information is summarized from Bettiol et al. (2008), Loeppert and Inskeep (1996), and Raiswell et al. (1994).

Iron present in suspended coastal marine and aquatic particles and sediments can take a number of forms, which are summarized in Fig. 1 in relation to analytical methods relevant to this study. In oxygenated waters, ferric (+3 oxidation state) iron can be present as oxides and hydroxides of varying crystallinity. At one extreme are poorly ordered, often freshly precipitated amorphous iron oxide and hydroxides, sometimes present as coatings on other particles (Babin and Stramski 2004). At the other are well-ordered iron oxide minerals such as hematite ($\alpha$-$Fe_2O_3$) and goethite ($\alpha$-FeOOH). Under reducing conditions, ferrous (+2 oxidation state) iron can be present as monosulfides (FeS), pyrite ($FeS_2$), and siderite ($FeCO_3$). Clay minerals (aluminosilicates composed of sheet-like layers) may also contain iron, present within the sheet structure or between the layers. Reductive extractions are often used to selectively isolate the easily reducible, ferric iron oxides and hydroxides listed above, while concentrated-acid extractions additionally remove carbonates, monosulfides, and some silicate and aluminosilicate iron (Raiswell et al. 1994). In this study, we use information from both types of extractions to examine the influence on $a_p^*(\lambda)$ of not only the amount, but the form of iron in coastal marine and aquatic particles.

Particulate organic matter and iron oxides may often be transformed together in estuaries and coastal sediments through processes including aggregation (Mayer 1982), photochemical reaction (Estapa and Mayer 2010), and microbial metabolism (Canfield 1989). In this study, we set out to determine whether POC and iron oxide content could explain optical absorption of mostly mineral particles that are typically encountered in a large subtropical river and coastal system, the coast of Louisiana. We also show that methods utilizing chemical or thermal oxidation of particles to remove OC or phytoplankton pigments may change iron-related absorption properties. Finally, we demonstrate the connection between suspended mineral particle absorption, which is a growing area of interest in hydrologic optics, and established chemical extraction techniques, which have been used for decades in studies of coastal iron and OC diagenesis. Clarification of the roles of concentration and phase of iron minerals in suspended particle absorption will permit us to develop a better mechanistic understanding of particulate photochemical reactions in coastal areas (Mayer et al. 2006) and, conversely, will perhaps shed light on transport and transformations of iron oxides at interfaces between rivers and the ocean.

## Methods

*Study area and sample collection*—The Atchafalaya Bay complex of coastal Louisiana (Fig. 2) is a shallow, river-dominated, low-gradient coastal system characterized by episodic, wind-driven sediment resuspension (Allison et al. 2000). It receives high inputs of suspended particles from

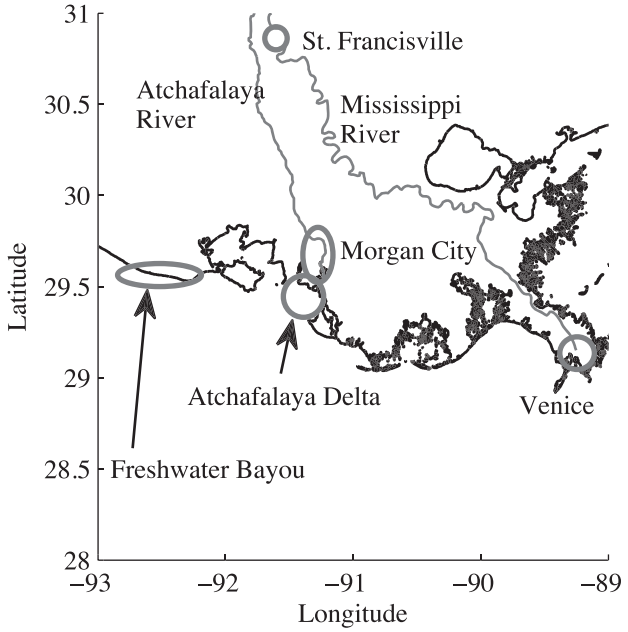


Fig. 2. Map of study area showing approximate locations of suspended particle and sediment sample collection (labeled gray ovals).

the Atchafalaya River, which are carried westward along the coast. To the east lies the delta of the Mississippi River, which drains a large fraction of the North American continent and, together with its distributary, the Atchafalaya, delivers large sediment loads to the Gulf of Mexico. Unconsolidated, surficial bottom sediments analyzed here were collected at the Atchafalaya River delta and near Freshwater Bayou (Fig. 2). Suspended particle samples were isolated from turbid waters via large-volume settling and centrifugation from the Atchafalaya River at Morgan City, Louisiana, from the Mississippi River at St. Francisville and Venice, Louisiana, and from surface waters near Freshwater Bayou (Fig. 2). Sodium chloride and magnesium sulfate salts were added to settling samples to induce aggregation and speed the particle collection process. Conditions were sufficient to collect particles larger than 1 $\mu$m, based on Stokes' Law calculations, but smaller particles were also likely to have been collected within settling aggregates. After final centrifugation and removal of supernatant, the residual (based on salt content) seawater contributions of dissolved iron and OC were negligible. Samples were collected in many separate trips during 2003–2008. All were freeze-dried shortly after collection and stored frozen until analysis in 2008 and 2009. Samples were covered during freeze-drying and were transferred in large enough quantities that losses of fine particles relative to coarser ones were likely negligible. No attempt was made to extract phytoplanktonic pigments from the samples, although pigment-specific absorption features, in particular the red peak associated with residual chlorophyll (Chl) *a* and its detrital products, were negligible. This may have been due to low pigment content or rapid degradation of pigments after damage to cells (Stramski 1990), which would have occurred during treatments listed above.

*OC and iron analyses*—OC content of each sample was measured on subsamples via combustion and quantification of $CO_2$ gas (Perkin-Elmer 2400B Elemental Analyzer) after 24 h of vapor-phase acidification (concentrated HCl) to remove carbonates. Precision of OC analyses was $\pm$ 0.1 mg OC per gram dry sediment (hereafter, $g^{-1}$). HCl-extractable iron content ($Fe_{mHCl}$) of subsamples (not the same ones used for OC analysis) was determined by inductively coupled plasma–atomic emission spectroscopy (ICP-AES) after closed-vessel microwave digestion with concentrated HCl (referred to here as "acid-extracted"; Link et al. 1998). Uncertainty of $Fe_{mHCl}$ measurements (based on replicate extractions of selected samples) was $\pm$ 0.02 wt% Fe. Shorter open-vessel reactions with boiling HCl typically extract the iron oxides, carbonates, and acid-soluble monosulfide minerals, as well as some iron-containing sheet silicate minerals such as nontronite (Fig. 1; Raiswell et al. 1994). The longer, higher-temperature and -pressure, closed-vessel treatments used here likely also extracted sheet silicate iron from chlorites, as well as partially recovered pyrite iron (Fig. 1; Bettiol et al. 2008). Crystalline and amorphous iron oxides and organic-iron complexes ($Fe_{dith}$; Fig. 1) were extracted at pH 3.5 via the dithionite–citrate method (referred to here as "dithionite-extracted"; Loeppert and Inskeep 1996), and extracts were analyzed for iron via ICP-AES. Analytical error in $Fe_{dith}$ for dithionite extraction and ICP analysis was $\pm$ 0.06 wt% Fe (based on replicate extractions of selected samples). Residual dithionite-extracted sediments were repeatedly rinsed with MilliQ® water and centrifuged to remove residual citrate and sulfates and then were freeze-dried and stored frozen.

*Absorption measurements and data analysis*—Sediment and suspended particle samples were gently hand-ground with a Diamonite® mortar and pestle to break up flakes formed during freeze-drying, passed through a 63-$\mu$m sieve, homogenized, and then weighed and resuspended in MilliQ® water to give a mass concentration of approximately 500 $\pm$ 2 mg $L^{-1}$. Samples were ground and sieved in sufficient quantities to minimize particle size–dependent losses during transfers. The suspension concentration was high enough to render negligible any sample-blank differences in back-reflection from cuvette walls (Babin and Stramski 2002; Stramski et al. 2007), minimize the effects of random weighing and subsampling errors in calculated suspension mass concentrations, and give sufficient absorbance signal-to-noise ratios to allow derivative analysis of the spectra (below). At the same time, the particle concentration was low enough to minimize effects of multiple scattering within the cuvette (ascertained up to optical densities of 0.2 at 400 nm using dilution series of representative samples; not shown). To maximize disaggregation, we gently mixed suspensions for at least 8 h and then ultrasonicated them for 20 min (Sonics VC505) immediately prior to measurement. Each ultrasonicated suspension was hand-mixed until visually homogenized and

pipetted into a 1-cm quartz fluorescence (four clear sides) cuvette fitted with a mechanical stirrer.

We scanned each suspension for absorbance vs. wavelength in a 15-cm diameter, centered sample-mount integrating sphere (Labsphere DRA-CA-3300) interfaced to a benchtop spectrophotometer (Cary 300). This measurement geometry has previously been shown to eliminate the need for correction of absorption data for scattering losses (Babin and Stramski 2002). Suspensions were stirred for the ~ 5-min duration of each absorbance scan to prevent particles from size-sorting or aggregating and settling out of the light beam during measurements. Inside the integrating sphere, all exposed stirrer surfaces were covered with clean white Teflon tape to minimize absorption, and sample scans were blanked against room-temperature MilliQ® water stirred at the same rate as the sample. We also resuspended selected marine samples in artificial seawater and dilute $CaCl_2$ to determine whether optical effects arose from the salinity change in MilliQ® water. However, measured absorption was not affected as long as samples were handled as described above. Each suspension was scanned in triplicate from 300 nm to 800 nm, and mass-specific absorption was computed according to Eq. 1 below, in which $A(\lambda)$ is the mean, blank-corrected absorbance for a sample suspension, $l$ is the cuvette path length (m), and [SPM] is the particle mass concentration (g $m^{-3}$)

$$a_p^*(\lambda) = \frac{2.303 \times A(\lambda)}{l \times [\mathrm{SPM}]} \quad (1)$$

Wavelength-dependent analytical error in mass-specific absorption ($m^2$ $g^{-1}$) was computed as twice the standard deviation of replicate scans for each sample. Relative error due to uncertainty in SPM concentration was negligible.

Spectral slopes were computed from $a_p^*$ spectra by nonlinear fitting to a single-exponential decay function (Eq. 2) over two wavelength ranges, 400–800 nm and 300–800 nm, yielding two spectral slope parameters ($S_{VIS}$ and $S_{UV\text{-}VIS}$, respectively).

$$a_p^*(\lambda) = A \times e^{(-S \times (\lambda - 400))} + B \quad (2)$$

The $B$ term in Eq. 2 corresponds to a positive offset at near-infrared wavelengths. While typically nonstandard in computations of CDOM spectral slope, the extra term was added here because the single-exponential function otherwise poorly fits the data in the presence of occasionally observed nonzero near-infrared absorption by mineral particles (Babin and Stramski 2004; Doxaran et al. 2009), which at 800 nm averaged 0.008 ± 0.004 $m^2$ $g^{-1}$ (two standard deviations) over the whole sample set. Uncertainty in spectral slope was computed by Monte Carlo propagation of analytical error in $a_p^*$ measurements.

To examine second-order features in $a_p^*$ spectra, first- and second-derivative absorption spectra were computed (Kosmas et al. 1984). We first applied a 30-nm, zero-phase distortion boxcar filter (Matlab® routine "filtfilt.m") to the absorption spectra to smooth noise, discarding the lowest and highest 15 nm from each spectrum. The selected filter width was the narrowest that provided acceptable signal-to-noise in the second-derivative spectra. Next, the first derivative ($da/d\lambda$) was computed in 1-nm steps by finding the slope of the best-fit line over a 10-nm interval (reported at the center wavelength of each interval). Finally, we repeated the differentiation step above to calculate second-derivative spectra ($d^2a/d\lambda^2$) from the first derivatives. Error in the first and second derivatives was estimated by propagating the analytical error from the $a_p^*$ measurements.

*Oxidation and reduction treatments*—Effects of oxidative, organic matter–removal treatments on mass-specific absorption were assessed qualitatively through coupled optical measurements and experimental treatments. OC was oxidatively removed via three different treatments: (1) freeze-dried, gently-ground sediments were subjected to thermal combustion for 8 h at 350°C in air (Mitchelson et al. 1986); (2) suspended sediments were oxidized in bicarbonate-buffered (pH ~ 8.5) solutions of potassium persulfate at 80°C for periods of 20 min, 2 h, and 21 h (Meier and Menegatti 1997); and (3) stirred, suspended sediments were exposed to 254-nm irradiation from an unfiltered mercury vapor lamp (UV Solutions) at room temperature for periods of 2 and 6 d. Control extractions for the latter two treatments included heating suspensions in MilliQ® water at 80°C and stirring suspensions in the dark for 2 d or 6 d, respectively. To show the effect of dithionite–citrate iron extraction on particle absorption coefficients, and to examine effects of OC removal in the absence of $Fe_{dith}$, sediments were sequentially subjected to dithionite–citrate extraction (Loeppert and Inskeep 1996), rinsed as described above, and then reoxidized either with persulfate (Meier and Menegatti 1997) or with simulated sunlight (Suntest XLS+, Atlas). All treated samples were rinsed with MilliQ® water (if in aqueous suspension), centrifuged, and freeze-dried prior to being resuspended and scanned in the integrating sphere as described above.

## Results

*Mass-specific absorption*—Absorption spectra of suspended particles and sediment samples from coastal Louisiana and the Mississippi and Atchafalaya Rivers were similar to suspended particles from other coastal marine environments, although many spectra displayed slight shoulders at ~ 360–390 nm and ~ 400–450 nm (Fig. 3). Characteristic Chl *a* absorption peaks were not observed in any of the sample spectra, consistent with similar suspended and sedimented samples' average Chl contents (7.5 μg Chl $g^{-1}$; data not shown), whose contribution to mass-specific absorption at 440 nm would be smaller than the measurement uncertainty, assuming a conservatively high value (0.1 $m^2$ mg $Chl^{-1}$) for Chl-specific absorption. The magnitude of $a_p^*(\lambda)$ ranged between 0.12 $m^2$ $g^{-1}$ and 0.34 $m^2$ $g^{-1}$ at 300 nm and between 0.01 $m^2$ $g^{-1}$ and 0.05 $m^2$ $g^{-1}$ at 550 nm. Differences between $a_p^*$ spectra of sediments and suspended particles could not be tested because no freshwater sediment (river-bottom) samples were collected. Among suspended particle samples only, the mean $a_p^*$ spectrum did

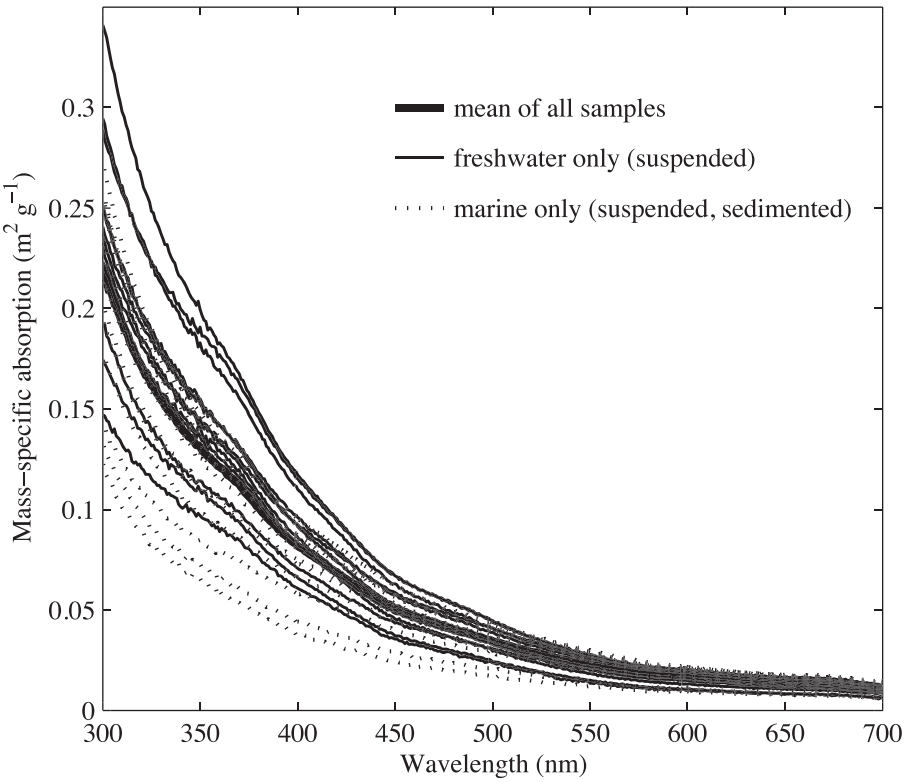


Fig. 3. Mass-specific absorption spectra of all samples analyzed here ($n = 25$). Heavy black line shows the mean, thin solid lines show samples from freshwater sites on the Atchafalaya and Mississippi Rivers, and dashed lines show samples from marine sites at Freshwater Bayou and the Atchafalaya River delta. River samples are suspended particulates only; marine samples include both sediments and suspended particulates.

not differ significantly at any wavelength as a function of season, year, or individual sample site, although the samples with the largest absorption coefficients were collected in freshwaters in the springtime. The mean $a_p^*$ spectrum for suspended particle samples pooled from all freshwater locations (St. Francisville, Venice, and Morgan City) was significantly different, at wavelengths between 328 nm and 396 nm and greater than 598 nm, from suspended particle samples pooled from the marine (and counterintuitively named) Freshwater Bayou site (Fig. 4; two-tailed $z$-test, $\alpha = 0.05$).

*OC and iron*—OC contents of sediments ranged from 1% to 3% by weight (12–31 mg OC $g^{-1}$). Riverine suspended particle samples had the highest OC contents, and marine sediments had the lowest. A positive but weak relationship ($R < 0.65$ at all wavelengths, $p < 0.05$ at wavelengths less than 575 nm) existed between $a_p^*(\lambda)$ and the OC contents of all samples (Figs. 5A, 6). Acid-extractable iron contents ($Fe_{mHCl}$; Fig. 1) ranged between 2.31 wt% Fe and 4.78 wt% Fe. The relationships between $a_p^*$ and $Fe_{mHCl}$ for freshwater and marine samples exhibited apparently similar slopes with different intercepts (Fig. 5B), but comparisons of the two sample groups' regression parameters were not statistically significant due to the poor fit of low-$Fe_{mHCl}$ marine sediment samples to the linear model and because of the small $Fe_{mHCl}$ range in marine suspended particle samples. Type-II linear regressions between OC and $a_p^*(350)$ and $Fe_{mHCl}$ and $a_p^*(350)$ both had negative intercepts, suggesting the presence of nonabsorbing OC and $Fe_{mHCl}$ subpools (Fig. 5A,B).

Dithionite-extractable iron contents ($Fe_{dith}$; Fig. 1) ranged between 1.04 wt% and 2.93 wt%, accounting for 30–67% of measured $Fe_{mHCl}$. While OC and $Fe_{dith}$ were not strongly correlated ($R = 0.5$, $n = 22$, $p < 0.05$, data not shown), $Fe_{dith}$ and $a_p^*$ exhibited a strong correlation ($R > 0.8$) at all wavelengths below 445 nm, with a maximum of $R = 0.91$ at 358 nm (Figs. 5C, 6A). The correlation between $Fe_{dith}$ and $a_p^*$ was significant at wavelengths less than 575 nm and highly significant ($p < 10^{-4}$) in the UV and blue portions of the spectrum (Fig. 6B). At 350 nm, the $y$-intercept of the Type-II linear regression between $a_p^*$ and $Fe_{dith}$ was not significantly different from zero (Fig. 5C; $p < 0.05$), suggesting that the entire dithionite-extractable iron pool contributed to the measured absorption.

Finally, the portion of the $Fe_{mHCl}$ pool not extractable by dithionite (denoted as $[Fe_{mHCl} - Fe_{dith}]$, and presumed to include iron monosulfides, carbonates, the more soluble silicate iron minerals, and possibly some pyrite iron; *see* Fig. 1) was calculated for each sample as the difference between the two iron measurements. This pool was poorly correlated with $a_p^*(350)$ over the whole sample set and within subgroups, but freshwater suspended particle samples had lower $[Fe_{mHCl} - Fe_{dith}]$ values than did

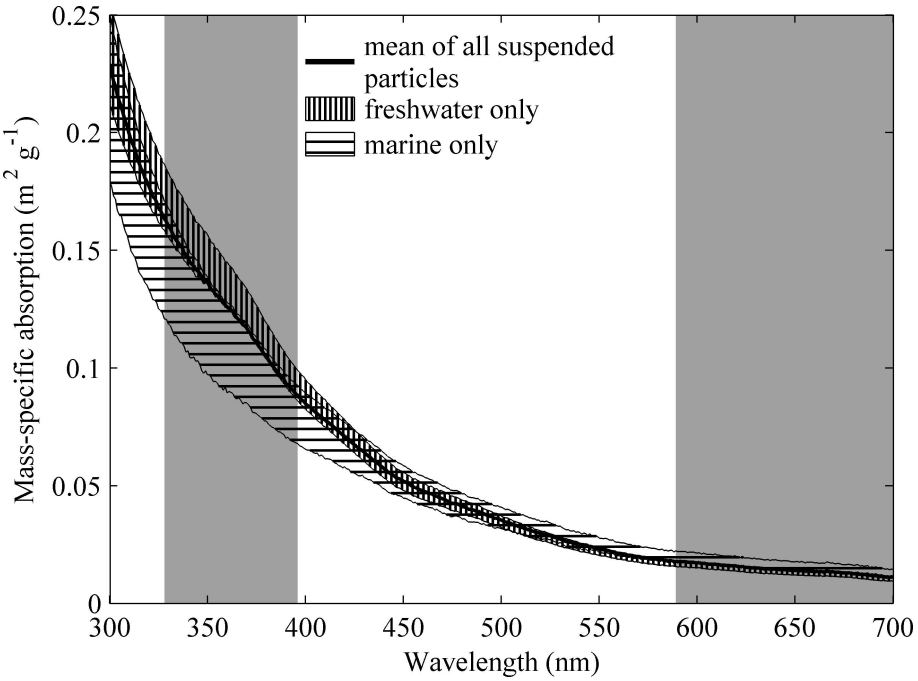


Fig. 4. Mean mass-specific absorption spectra for suspended samples from freshwater vs. marine sites. Heavy black line shows the mean spectrum for all samples. Vertically hatched area shows 95% confidence interval for the mean spectrum of freshwater samples, while horizontally-hatched area shows 95% confidence interval for the mean spectrum of marine samples. Gray-shaded background areas denote wavelength regions where the mean spectra of freshwater and marine samples differed significantly ($z$-test, $\alpha = 0.05$).

marine suspended particles (Fig. 5D). The correlation between [$Fe_{mHCl} - Fe_{dith}$] and $a_p^*$ was insignificant ($p > 0.1$) at wavelengths less than 508 nm but strengthened at red and near-infrared wavelengths, reaching a maximum of $R = 0.78$ at 780 nm (Fig. 6).

*Spectral slopes*—The mean spectral slope for the entire sample set of particulates measured here was not significantly different when calculated over two different wavelength intervals (two-tailed $z$-test, $\alpha = 0.05$). Over the 300–800 nm interval, $S_{UV\text{-}VIS}$ was $0.0101 \pm 0.0006$ nm$^{-1}$, while over the 400–800 nm interval, $S_{VIS}$ was $0.0104 \pm 0.0009$ nm$^{-1}$. Freshwater samples had significantly higher values of $S_{VIS}$ ($0.0111 \pm 0.0007$ nm$^{-1}$, 1 SD, $n = 14$) than did marine samples ($0.0097 \pm 0.0004$ nm$^{-1}$, $n = 13$), but there was no difference in $S_{UV\text{-}VIS}$ between the sample groups (two-tailed $z$-test, $\alpha = 0.05$; Fig. 7). Analytical error in $S_{UV\text{-}VIS}$ and $S_{VIS}$ (based on $a_p^*$ uncertainty) was 0.0001 nm$^{-1}$. Freshwater samples' $S_{VIS}$ values ranged from 1% to 21% higher than their $S_{UV\text{-}VIS}$ values, while marine samples' $S_{VIS}$ values ranged from 10% lower to 3% higher than their corresponding $S_{UV\text{-}VIS}$ values. The spectral slope parameter $S_{UV\text{-}VIS}$ was not significantly correlated to OC or $Fe_{dith}$ content, although the highest $S_{UV\text{-}VIS}$ values (greater than 0.011 nm$^{-1}$) included the lowest OC and $Fe_{dith}$ marine sediment samples (Fig. 7A,B). In marine samples only, $S_{VIS}$ values were similarly correlated to OC content ($R = 0.64$, $p = 0.02$, $n = 12$; Fig. 7C) and to $Fe_{dith}$ content ($R = -0.63$, $p = 0.05$, $n = 10$; Fig. 7D).

*Oxidation and reduction treatments*—Removal of OC by various methods resulted in small and inconsistent changes in mass-specific absorption (Fig. 8). Thermal combustion, which removed 80% of the initial OC, increased $a_p^*$ slightly at wavelengths between 320 nm and 600 nm (Fig. 8A), while potassium persulfate oxidation, which removed 88% of the initial OC, caused a large increase in $a_p^*$ below 450 nm and a small decrease above 450 nm (Fig. 8B). Mass-specific absorption decreased slightly at wavelengths above 350 nm, and OC decreased by 41% during UV irradiation (Fig. 8C).

Reductive dithionite extraction of iron oxides in marine sediment removed only 1% of initial OC (the C : N ratio of organic matter remained constant, so replacement of sample OC with citrate could not have been greater than $\sim$ 10%, taking into account analytical precision), but $a_p^*$ was reduced by over 50% at wavelengths below 700 nm (Fig. 9). Subsequent persulfate reoxidation caused a loss of 81% of the initial OC and a small decrease in $a_p^*$ at all wavelengths, while photochemical reoxidation of a separate, dithionite-reduced subsample resulted in a smaller loss of only 14% of initial OC, and a small increase in $a_p^*$ at all wavelengths (Fig. 9).

*Spectral absorption second derivatives*—Second derivatives of $a_p^*$ spectra ($d^2a/d\lambda^2$) showed absorption features at wavelengths coincident with the electronic transitions of iron oxide minerals (Fig. 9; Sherman and Waite 1985). Valleys in $d^2a/d\lambda^2$ correspond to the locations of weak shoulders in the original absorption spectra. The sizes of

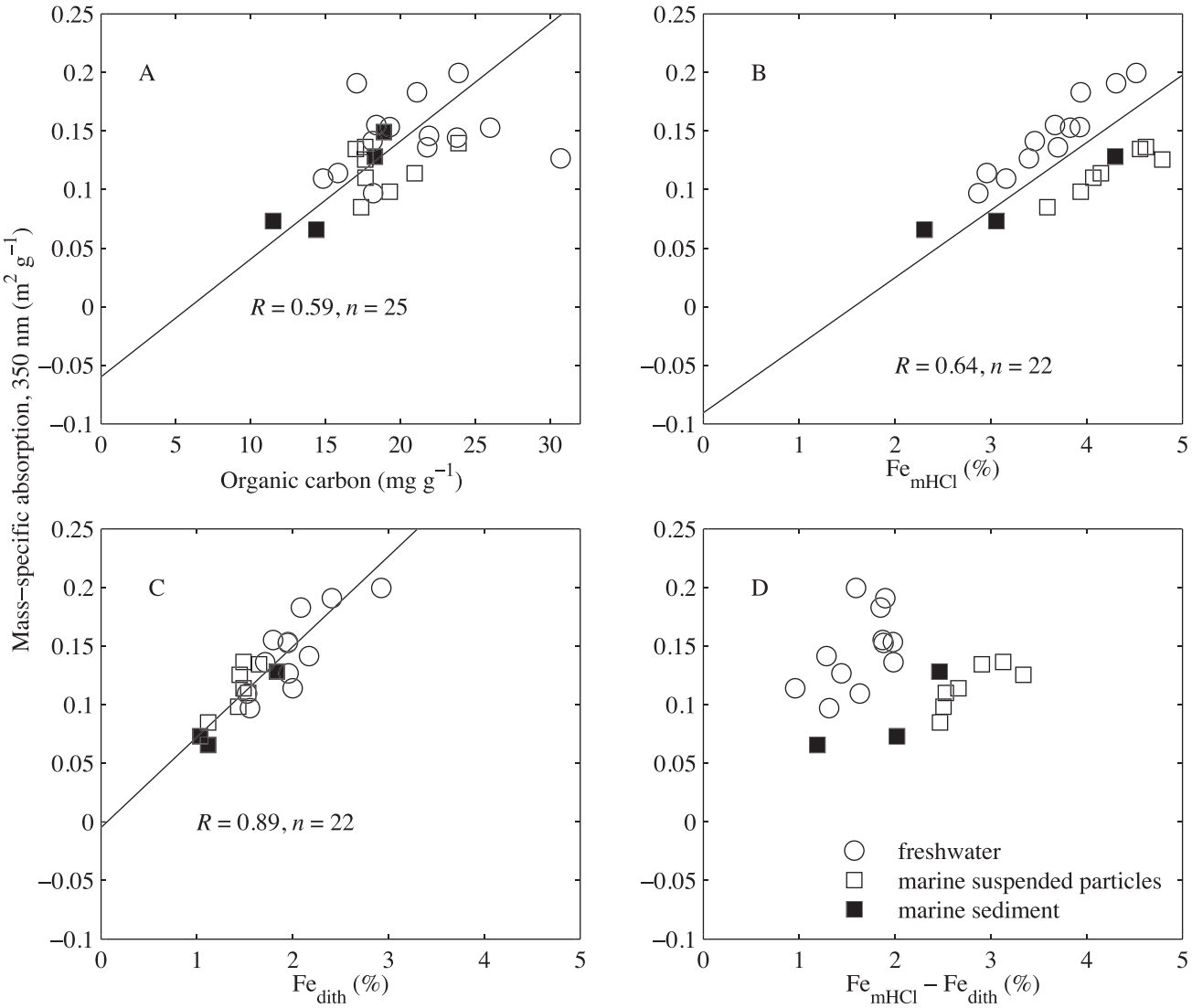


Fig. 5. Mass-specific absorption at 350 nm vs. measured compositional parameters (each symbol represents an individual sample). Circles show freshwater, and squares show marine samples. Open symbols are suspended particles, filled symbols are sediments. (A) $a_p^*(350)$ vs. organic carbon content (mg OC $g^{-1}$). Type-II regression: $a_p^*(350) = (0.010 \times OC) - 0.06$, $R = 0.59$, $n = 25$. Point with organic carbon content of 31 mg $g^{-1}$ is excluded from regression. (B) $a_p^*(350)$ vs. concentrated, microwave HCl-extracted iron ($Fe_{mHCl}$, weight percent). Type-II regression: $a_p^*(350) = (0.058 \times Fe_{mHCl}) - 0.09$, $R = 0.64$, $n = 22$. (C) $a_p^*(350)$ vs. dithionite-extracted iron ($Fe_{dith}$, weight percent). Type-II regression: $a_p^*(350) = (0.077 \times Fe_{dith})$, $R = 0.89$, $n = 22$. (D) $a_p^*(350)$ vs. the difference [$Fe_{mHCl} - Fe_{dith}$]. Linear correlation between $a_p^*(350)$ and [$Fe_{mHCl} - Fe_{dith}$] is insignificant at 350 nm (*see* Fig. 6).

the shoulders at 382 nm and 435 nm (Fig. 3) were computed by taking the difference between adjacent minima and maxima in the second-derivative spectra. These differences should obey Beer's Law and are respectively termed $\Delta a_{2d}(382)$ and $\Delta a_{2d}(435)$. For ease of computation, fixed minimum and maximum wavelength pairs of 368, 395 nm and 423, 446 nm were used (Fig. 10). Second-derivative differences $\Delta a_{2d}(382)$ and $\Delta a_{2d}(435)$ were not well correlated to sample OC content ($R = 0.34$ and 0.52, respectively; Fig. 11A,C), and the slopes of the respective regression lines were not significantly different from zero ($p < 0.05$). However, both parameters showed a linear relationship with $Fe_{dith}$ ($R = 0.85$ and $R = 0.83$, respectively; Fig. 11B,D). Corresponding linear regressions against $Fe_{dith}$ exhibited positive slopes, but only the negative intercept of $\Delta a_{2d}(382)$ vs. $Fe_{dith}$ was significantly different than zero ($p < 0.05$).

## Discussion

Spectral $a_p^*$ varied by a factor of 1.5–1.7 among samples measured, a far smaller range than the orders-of-magnitude variations in suspended particulate matter (SPM) concentration observed along the Louisiana coast (Kineke et al. 2006). Therefore, the total absorption coefficient in the coastal water column is likely to be far more sensitive to SPM concentration than to variations in the mass-specific absorption of the particles. However, given the SPM levels

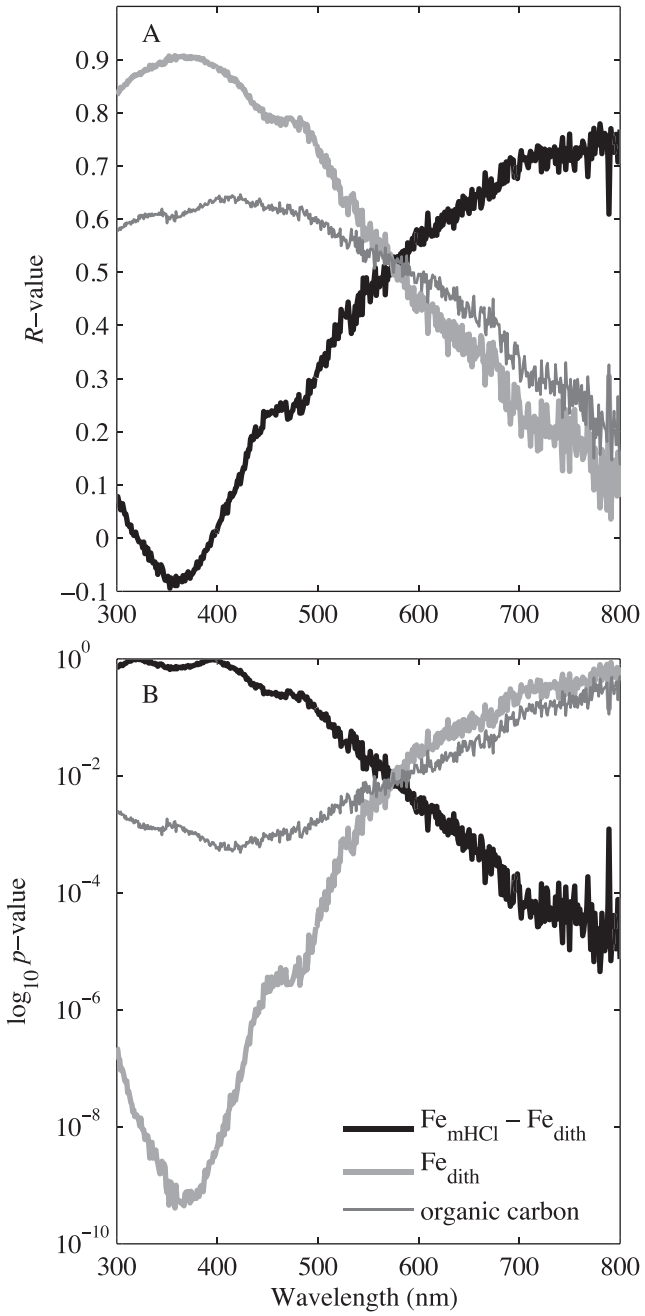


Fig. 6. (A) Linear correlation coefficient ($R$) between compositional parameters and mass-specific absorption, for all samples plotted in Fig. 5, as a function of wavelength. Freshwater and marine samples were not separated in this analysis. High organic carbon (31 mg OC $g^{-1}$) sample excluded from Fig. 5 regression is also excluded here. Thick black line shows correlation between $a_p^*(\lambda)$ and [$Fe_{mHCl} - Fe_{dith}$]; thin dark-gray line shows correlation between $a_p^*(\lambda)$ and $Fe_{dith}$; and thick light-gray line shows correlation between $a_p^*(\lambda)$ and organic carbon. (B) $\log_{10}$ of the $p$-value for the linear correlation between absorption and composition as a function of wavelength, with line shading as in upper panel.

typically encountered in the Atchafalaya Bay region ($10^1$–$10^3$ g $m^{-3}$; Kineke et al. 2006) and the magnitude of $a_p^*(\lambda)$ reported here, we expect the relative contribution of suspended particles to the total absorption coefficient to be quite high. In a 2-yr field study of shallow waters within 5.6 km of the Louisiana coast, conducted by Schaeffer et al. (2011), the absorption coefficient of CDOM (the other main contributor to absorption) was rarely larger than 10 $m^{-1}$ at 412 nm; and, consistent with our $a_p^*$-based prediction, particles often dominated total absorption. Similar high contributions of particles to total absorption have been reported globally, including near the Amazon River delta in the western tropical North Atlantic (Del Vecchio and Subramaniam 2004), in European and Arctic coastal waters (Bélanger et al. 2008), and at Imperial Beach, California (Woźniak et al. 2010). Wavelength-dependent processes such as photodegradation of POC and DOC, whose rates scale directly with light absorption by particulate matter, may, in addition, be sensitive to the relative spectral slopes of CDOM and particulate absorption.

Mass-specific particle absorption at 440 nm measured for these Louisiana coastal particles (mean ± 1 SD = 0.056 ± 0.012 $m^2$ $g^{-1}$) overlaps the distribution of $a_p^*$(440 or 443) values reported for other mostly mineral, coastal marine and freshwater particles from a range of locations (mean ± 1 SD = 0.062 ± 0.013 $m^2 g^{-1}$; Bowers and Binding 2006). Values reported here agree well with $a_p^*$(440) data of Snyder et al. (2008) for the nearshore, northern Gulf of Mexico site at Mobile Bay (mean ± 1 SD = 0.05 ± 0.01 $m^2$ $g^{-1}$), and are encompassed by the larger range of $a_p^*$(443) (0.012–0.079 $m^2$ $g^{-1}$) computed from the data of D'Sa et al. (2006) for nonalgal particles collected just to the west of the Mississippi River delta. The lowest values of D'Sa et al. (2006) are much smaller than we report here, but Wozniak et al. (2010) showed that $a_p^*(\lambda)$ varies inversely with the POC : SPM ratio in suspended particles from their Imperial Beach, California, site. While D'Sa et al. (2006) do not report POC, their samples had Chl : SPM ratios on the order of $10^{-3}$, which is much higher than our samples (Chl : SPM ~ $10^{-6}$) and suggests a higher POC content. Values of $S_{VIS}$ (mean ±1 SD for all samples = 0.0104 ± 0.0009 $nm^{-1}$) are also consistent with previous values reported in the literature for nonalgal particles (Babin et al. 2003).

Non-compositional factors likely to have affected the magnitude of $a_p^*(\lambda)$ include the particle size distribution (PSD; Stramski et al. 2007; Woźniak et al. 2010) and aggregate size distribution (ASD) of our sediment and suspended particle samples. For the purposes of discussion, we define ASD as the in situ size distribution of aggregated particulate material and PSD as the size distribution of that same material broken down into primary particles. PSD affects $a_p^*(\lambda)$ because absorbing material in the solid interior of larger particle packages is "shaded" to a greater extent than in smaller particles (Duysens 1956). In this study, we did not preserve the in situ size distributions of aggregates or primary particles, but took precautions against preferential loss of small-sized, optically important primary particles by avoiding size fractionation during

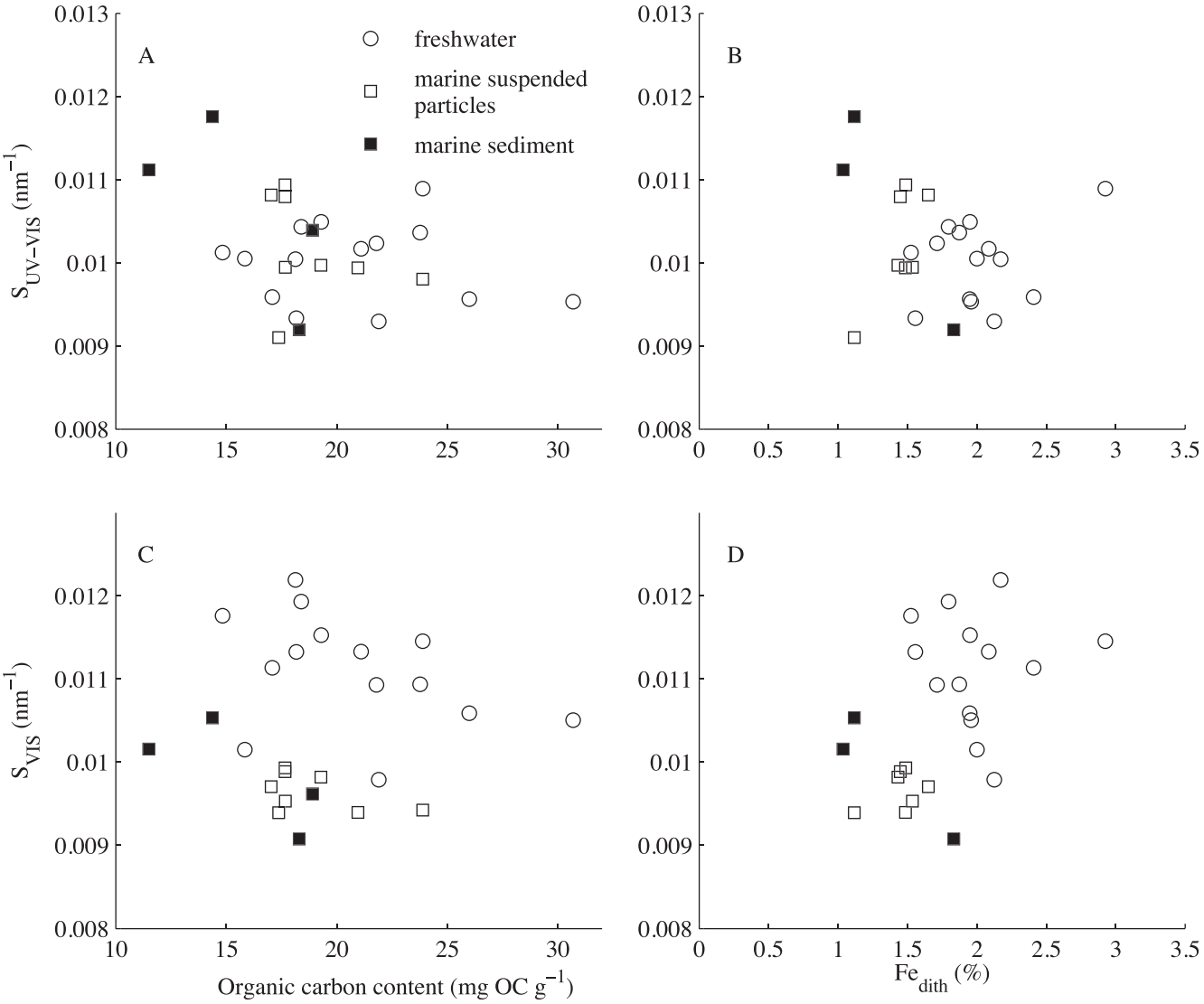


Fig. 7. Spectral slopes computed by nonlinear fit to Eq. 2 over the wavelength range 300–700 nm ($S_{UV-VIS}$) or 400–700 nm ($S_{VIS}$) as a function of dithionite-extractable iron and organic carbon contents. Circles show freshwater samples, squares show marine samples, open symbols show suspended particles, and filled squares show sediments. (A) $S_{UV-VIS}$ vs. organic carbon; (B) $S_{UV-VIS}$ vs. $Fe_{dith}$; (C) $S_{VIS}$ vs. organic carbon; (D) $S_{VIS}$ vs. $Fe_{dith}$. Freshwater and marine samples are not significantly different when exponential spectral slope is computed from 300–700 nm, but the two groups sort differently as a function of both $Fe_{dith}$ and OC when the 400–700 nm range is used for the calculation. In marine samples only, $S_{VIS}$ values were similarly correlated to OC content ($R = 0.64$, $p = 0.02$, $n = 12$; Fig. 7C) and to $Fe_{dith}$ content ($R = -0.63$, $p = 0.05$, $n = 10$; Fig. 7D).

sample preparation and measurement. We did not attempt to quantify the effect of packaging, for instance by size-sorting particles prior to optical measurements, because we also expected $a_p^*(\lambda)$ to vary indirectly as a function of primary particle size, due to the covariance of size and composition in mostly mineral samples. In the Mississippi River and the coastal Louisiana region, particle size is the best predictor of particle mineralogy (Johnson and Kelley 1984), and both mineral type and particle size exert important, but different, direct controls on optical properties (Egan and Hilgeman 1979; Babin and Stramski 2004; Stramski et al. 2007). Looking beyond mineralogy and direct size control of optical properties, there are indirect size controls: Mayer (1994) showed that, in marine sediments, OC content increases with particle surface area (and thus scales inversely with particle size), while Poulton and Raiswell (2005) showed that dithionite-extractable iron content increases in smaller size fractions of glacial and riverine suspended sediments.

The effect of ASD on $a_p^*(\lambda)$ has never been measured directly, in part because the currently available methods for measuring particle absorption could modify aggregates to some unknown degree via filtration or pumping. Methods exist to measure the mass-specific beam attenuation coefficient ($c_p^*$) without breaking aggregates, however, and Boss et al. (2009) showed experimentally and through optical modeling that aggregation alters $c_p^*$ (660) by factors of tens of percent relative to $c_p^*$(660) of primary particles.

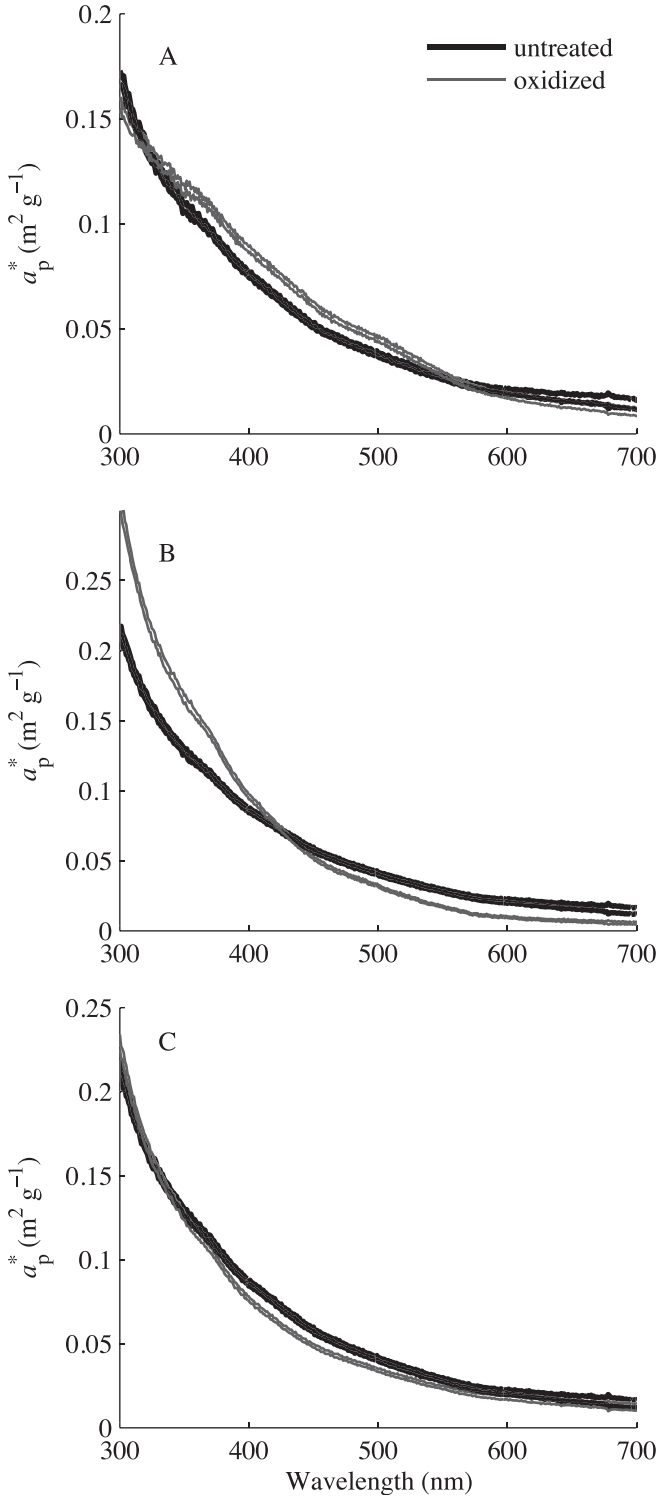


Fig. 8. Change in mass-specific absorption after oxidative treatment to remove organic carbon. Untreated absorption indicated by heavy black line, posttreatment absorption by thin gray line. (A) Combustion at 350°C for 8 h (loss of 80% OC). (B) Oxidation in bicarbonate-buffered potassium persulfate for 21 h at 80°C (loss of 88% OC). (C) Oxidation under UV light (254 nm mercury) for 6 d (loss of 41% OC).

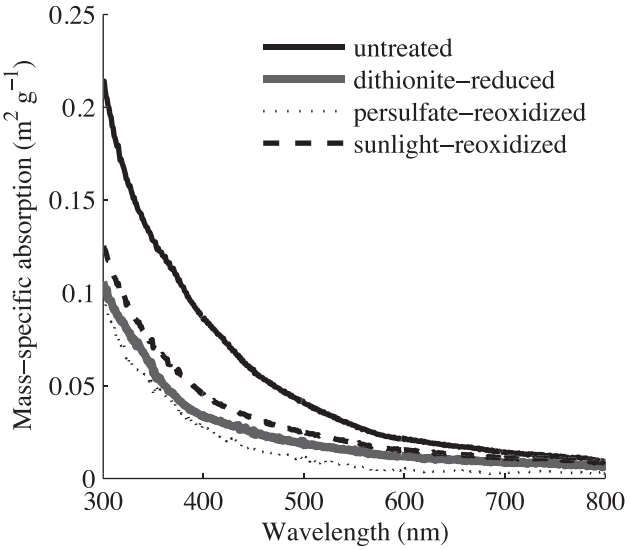


Fig. 9. Changes in mass-specific absorption during treatments to alter iron oxide absorption. Black line indicates untreated sample absorption, thick dark-gray line is absorption after dithionite reduction (loss of 1% OC), thin dotted line is absorption after reoxidation with potassium persulfate (further loss of 81% OC relative to dithionite treatment), and thick, dotted black line is absorption after reoxidation with simulated sunlight (24 h, further loss of 14% OC relative to dithionite treatment).

To similarly model the effect of aggregation on $a_p^*(\lambda)$, we applied the theory of anomalous diffraction (van de Hulst 1957) to estimate $a_p^*(\lambda)$ for hypothetical, environmentally relevant 10-, 100-, and 1000-$\mu$m diameter aggregates of 1-$\mu$m clay particles. We used complex refractive indices reported by Egan and Hilgeman (1979) for two clay samples: a more strongly absorbing, high-iron montmorillonite (imaginary refractive index of 0.0044 at 300 nm), and a less-absorbing kaolinite (imaginary refractive index of 0.0011 at 300 nm). The complex refractive indices of these model clays likely differ from those of our environmental samples but are similar enough to serve as a useful basis for our hypothetical model. Following Boss et al. (2009), we computed the aggregates' solid mass fractions from their diameters, according to the empirical model developed by Khelifa and Hill (2006).

The results showed that $a_p^*(\lambda)$ of aggregated clay particles can vary relative to disaggregated particles by tens of percent (similar to $c_p^*(660)$), with the most-pronounced effect occurring where the imaginary refractive index is highest, at UV wavelengths for the highly absorbing montmorillonite aggregates (Fig. 12A). Whether $a_p^*(\lambda)$ of aggregates is larger or smaller than $a_p^*(\lambda)$ of solid particles depends on aggregate size, solid fraction (Fig. 12), and primary particle size (not shown, but as in Boss et al. 2009). The difference between modeled $a_p^*(\lambda)$ of a single, 1-$\mu$m particle and 100- and 1000-$\mu$m aggregates was comparable to the difference between solid particles 1- and 10-$\mu$m in diameter (Fig. 12). While we could not preserve the in situ ASD during our absorption measurements, the model results in Fig. 12 show the importance of controlling this factor. We adopted sample handling

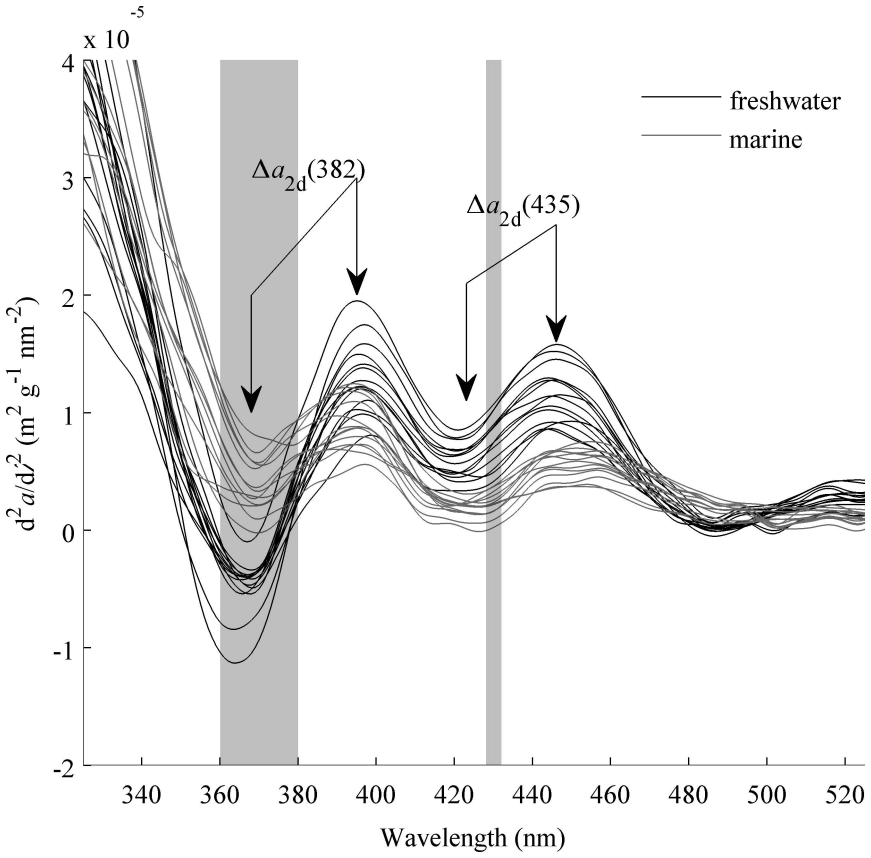


Fig. 10. Second derivatives of mass-specific absorption spectra. Black lines denote freshwater samples, and gray lines denote marine samples. Bracketed arrows labeled $\Delta a_{2d}(382)$ and $\Delta a_{2d}(435)$ show locations of second-derivative maxima and minima used to compute iron absorption peak heights plotted in Fig. 11. Light-gray vertical bars highlight approximate ranges for electronic transition bands of various iron oxide minerals (Sherman and Waite 1985).

methods described above (i.e., mixing and ultrasonication) for purposes of comparison within our study, because it was more practical to consistently maximize disaggregation of primarily mineral particles than to maintain a consistent state of aggregation among our samples. Thus, our reported $a_p^*(\lambda)$ values are likely maxima corresponding to fully or nearly fully disaggregated particles. The degree of measurement-related disaggregation affecting reported $a_p^*(\lambda)$ data in the literature is unknown but should be considered when comparing $a_p^*(\lambda)$ values among sites with contrasting in situ ASDs, or among studies where different sample handling methods were used.

The strong correlation between $a_p^*(\lambda)$ and dithionite-extractable iron ($Fe_{dith}$; Fig. 5C), the presence of features corresponding to iron oxide absorption bands (Sherman and Waite 1985) in our second-derivative spectra (Fig. 10), and the correlation between the size of these spectral features and $Fe_{dith}$ content of particles (Fig. 11B,D) all support a primary role for iron oxide and hydroxide minerals in light absorption by mostly inorganic marine particles from the terrestrially influenced coastal northern Gulf of Mexico. The strong role of $Fe_{dith}$ was apparent in our samples even without controlling or accounting for their particle size distributions. Also supporting this conclusion is the fact that dithionite extraction of the $Fe_{dith}$ pool from sediments caused a 50% reduction in $a_p^*(\lambda)$ that was not reversed by sunlight reoxidation (and thus was probably unrelated to redox alteration of non-$Fe_{dith}$ components; Fig. 9). Our data are consistent with the findings of Babin and Stramski (2004), who found strong iron-specific spectral absorption features and showed a positive but variable correlation between mineral iron content and $a_p^*(\lambda)$ of high-iron (5–29% by weight) dust and soil particles suspended in seawater. The lower iron contents of samples analyzed here are consistent with their less-prominent iron-specific absorption features, which we nonetheless have quantitatively related to dithionite-extractable iron mineral content using second-derivative analysis (Fig. 11B,D). These iron-specific absorption features also cause the spectral slope to change as a function of wavelength in the blue and UV parts of the spectrum.

It is unlikely that inorganic constituents, other than iron species discussed above, contribute significantly to $a_p^*$ values measured here. In addition to iron, the dithionite–citrate reduction method used here likely extracted some crystalline and amorphous oxides of aluminum (Bertsch and Bloom 1996) and manganese (Tessier et al. 1979), as well as trace transition metals and organic matter bound to the iron and manganese oxide phases (Tessier et al. 1979). Pure aluminum oxides themselves (neglecting transition

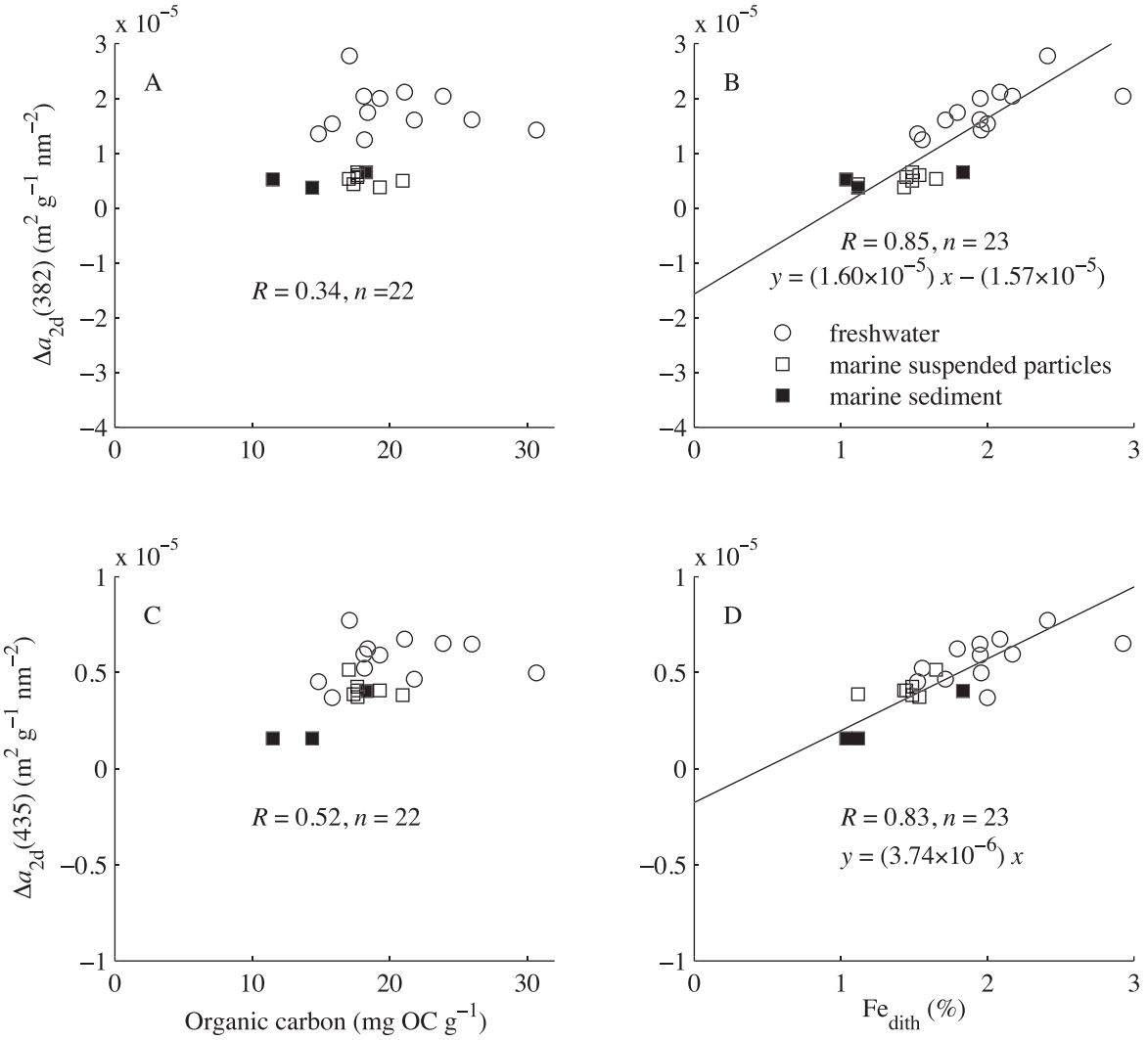


Fig. 11. Peak heights computed from second-derivative absorption spectra ($\Delta a_{2d}$) as a function of OC and $Fe_{dith}$ contents. Freshwater suspended particle samples shown by open circles, marine suspended particle samples by open squares, and marine sediments by filled squares. High organic carbon point (31 mg OC $g^{-1}$) is excluded from regressions against OC. (A) $\Delta a_{2d}(382)$ vs. organic carbon content. (B) $\Delta a_{2d}(382)$ vs. dithionite-extractable iron. (C) $\Delta a_{2d}(435)$ vs. organic carbon content. (D) $\Delta a_{2d}(435)$ vs. dithionite-extractable iron.

metal impurities, which are discussed separately below) do not absorb light except at high-energy vacuum-UV wavelengths not present at Earth's surface. Transition metals other than iron are expected to contribute to absorption features of natural minerals, but, because their contents are orders of magnitude smaller than that of iron in Mississippi River suspended sediments (Horowitz et al. 2001), their contributions to measured absorption are likely small. The results of Babin and Stramski (2004), who measured contents of a number of other transition metals in soil dust samples but found only iron to correlate well with $a_p^*$, support this assumption. Although dithionite may also dissolve ferric iron from some iron–organic complexes, prior studies of Mississippi watershed soils (Wagai and Mayer 2007) show minimal OC associated specifically with dithionite-extractable iron and manganese oxides.

The contribution of organic matter to the mass-specific spectral absorption of suspended coastal mineral particles is weaker than that of dithionite-extractable iron. The negative $y$-intercept and weak correlation in the linear regression of $a_p^*(350)$ against OC (Fig. 5A) suggest that a variable fraction of OC in these particle samples is non-absorbing at UV wavelengths. $Fe_{dith}$ and OC were only weakly correlated for our samples, which is consistent with the reported lack of sorptive association between dithionite-extractable iron and organic matter in soils from the Mississippi River watershed (Wagai and Mayer 2007). Our results, however, do not preclude absorption arising from non-sorptive interactions (complexation) of iron and organic matter (Fig. 1), and suspended mineral particles in other river systems may have different amounts of $Fe_{dith}$ : OC association. While our samples do not encompass a large range in POC content, our results are consistent with those of Woźniak et al. (2010), who observed an even weaker relationship between $a_p^*(400)$ and POC : SPM among samples from a single coastal site with both low ($< 0.06$) and high ($> 0.25$) POC fractions.

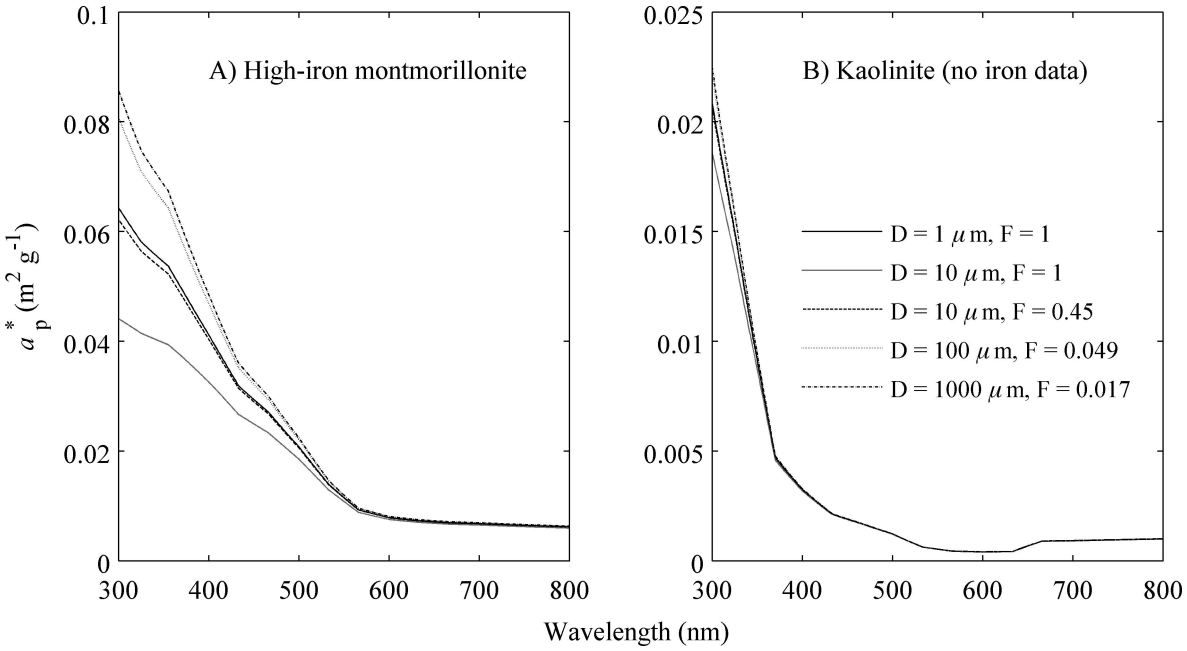


Fig. 12. Modeled effect of aggregation and primary particle size on mass-specific absorption by clay particles. Black and dark gray lines show single, solid particles, with 1-$\mu$m-diameter (D) particle in black and 10-$\mu$m particle in dark gray. Broken and light gray lines show 1-$\mu$m particles combined into model aggregates whose solid fractions (F) scale with aggregate diameter (D), according to the empirical model of Khelifa and Hill (2006). Heavy dashed line shows D = 10-$\mu$m aggregate with F = 0.45, light gray line shows D = 100-$\mu$m aggregate with F = 0.049, and light dashed line shows D = 1000-$\mu$m aggregate with F = 0.017. (A) Mass-specific absorption computed using imaginary part of refractive index measured on high (7.1 wt%) iron montmorillonite from Amory, Mississippi (Egan and Hilgeman 1979). (B) As in A, for kaolinite with unknown iron content from Macon, Georgia (Egan and Hilgeman 1979). Note scale difference between panels.

The changes in $a_p^*(\lambda)$ that resulted from oxidative OC removal from sediments (Fig. 8) were small, regardless of either the oxidation method used, or the prior removal of $Fe_{dith}$ (Fig. 9). The increases in $a_p^*(\lambda)$ observed during the heated oxidation treatments (combustion and persulfate oxidation) are also consistent with the simultaneous alteration of iron minerals. The response of iron oxide absorption bands to heat and oxidation treatments targeted at OC is of concern when those treatments are used to partition particulate absorption into its organic and inorganic components. The combustion method, for instance, has been previously noted to cause changes in particle absorption (Babin et al. 2003), specifically increasing absorption in the blue and decreasing absorption in the infrared (Werdell and Roesler 2003). To our knowledge, no study of the iron-related optical effects of oxidative, hypochlorite extraction of phytoplankton pigments (Ferrari and Tassan 1999) has been published. Gleyzes et al. (2002) suggested that sodium hypochlorite extraction is unlikely to attack amorphous oxyhydroxides or clay mineral–bound metals but that iron carbonate or sulfide minerals may be dissolved and the iron subsequently reprecipitated (*see* Fig. 1 for mineral relationships). Extraction of phytoplankton pigments in hot methanol (boiling point = 65°C; Kishino et al. 1985), while not an oxidizing treatment, could cause thermal alteration of iron oxides and hydroxides, some of which interconvert above temperatures of about 40°C (Schwertmann and Cornell 1991). While results of treatments here suggest that heat and oxidation treatments could alter optical properties of iron-containing minerals, more work is needed to test the iron-specific effects of common phytoplankton pigment extraction methods.

In our sample set, freshwater suspended particles collected from the Mississippi and Atchafalaya Rivers upstream of their deltas had enhanced $Fe_{dith}$ contents and iron-specific UV–blue absorption signatures, relative to marine suspended particles and sediments collected from the Louisiana inner shelf. The decrease in $Fe_{dith}$ is consistent with the data of Trefry and Presley (1982), who found constant total iron contents but progressively smaller amounts of dithionite-extractable iron (Fig. 1) in Mississippi River suspended particles, delta suspended particles, and delta sediments. Conversely, in our study the marine suspended particles and sediments had larger contents of HCl-extractable, but not dithionite-extractable, iron ($[Fe_{mHCl} - Fe_{dith}]$; Fig. 5D). This fraction probably included the iron monosulfide minerals and some pyrite iron (Fig. 1), which are the products of microbial sulfate reduction and dissimilatory iron reduction in low-oxygen sediments (Canfield 1989). Intense periodic resuspension of bottom sediments in the sampling region is common (Kineke et al. 2006), so suspended particles in marine waters of the inner shelf may also bear the signature of recent deposition in reducing sediments, where dithionite-extractable iron is transformed into reduced forms. Optical differences between freshwater and marine samples at UV–blue wavelengths are therefore consistent with iron reduction processes in marine sediments. These same processes produce increasing amounts of reduced-iron

minerals (e.g., monosulfides, carbonates, and some clays; Fig. 1) in marine sediments (Canfield 1989). It is thus intriguing that the correlation between [$Fe_{mHCl} - Fe_{dith}$] and mass-specific absorption reaches a maximum in the near-IR wavelengths (Fig. 6A), in the vicinity of a strong, broad, pyrite absorption band (maximum at ~1.7 eV ≈ 730 nm, approximate width of ± 150 nm; Bither et al. 1968). Clay minerals containing iron in both reduced ($Fe^{2+}$) and oxidized ($Fe^{3+}$) states, which could also be included in the [$Fe_{mHCl} - Fe_{dith}$] pool (Fig. 1), additionally exhibit a broad intervalence charge transfer band centered at 730 nm (Stucki and Lear 1989).

The dithionite-extractable iron pool is biogeochemically significant, both as a source of reducible iron for microbial communities (Canfield 1989) and photochemical reactions (Estapa and Mayer 2010). This component is also responsible for a significant portion of UV light absorption by particles. Under similar water-column particle loads, reduction of dithionite-extractable iron in suspended particles from 3% to 1% (river to marine) would result in the reduction of the particulate absorption coefficient by roughly 60% in the mid-UV wavelengths and 50% at 440 nm (the Chl *a* absorption peak). Especially in turbid waters where mineral particles dominate total absorption, increases in blue and UV light penetration would, respectively, have significant consequences for primary production and photochemical reactions.

We can also use dithionite-extractable iron to make predictions about regional variability in mineral particle absorption coefficients. Poulton and Raiswell (2002) tabulated dithionite-extractable iron contents of suspended particles from a global set of rivers. While they employed a milder version of the dithionite–citrate extraction (pH 4.8 for 1 h, rather than pH 3.5 for 24 h), which means their values of $Fe_{dith}$ are likely to be systematically lower than those reported here, we can speculate about global variability in coastal, mineral-particle $a_p^*(\lambda)$ values by considering the range of $Fe_{dith}$ reported by Poulton and Raiswell (2002). For suspended riverine particles, their $Fe_{dith}$ values vary from a low of 0.17% (Han River, Seoul, South Korea) to a high value of 4.93% (Tees River, Barnard Castle, United Kingdom). Using the $a_p^*(350)$:$Fe_{dith}$ relationship from coastal Louisiana (Fig. 5C), we derive local values of $a_p^*(350)$ of 0.013 $m^2\ g^{-1}$ and 0.38 $m^2\ g^{-1}$, for those respective sites. We can also estimate values for larger rivers, such as the Amazon ($Fe_{dith}$ = 2.60%, $a_p^*(350)$ = 0.20 $m^2\ g^{-1}$), the Huang He ($Fe_{dith}$ = 0.96%, $a_p^*(350)$ = 0.074 $m^2\ g^{-1}$), and the Brahmaputra ($Fe_{dith}$ = 0.62%, $a_p^*(350)$ = 0.048 $m^2\ g^{-1}$). While these predicted $a_p^*(350)$ values are probably biased low, the range of variability is consistent with $a_p^*(\lambda)$ measurements of terrestrial particles by Stramski et al. (2007), and the patterns of site-to-site differences could be testable with optical measurements.

In general, optical approaches allow us to observe processes at spatiotemporal resolutions that cannot be matched by analytical methods requiring discrete water samples. In situ optical observations thus have clear advantages in near-coastal and estuarine environments dominated by rapidly fluctuating tides, river discharge, and wind-driven processes. The optical measurements made in this study, conducted in the lab on discrete samples, point toward the design parameters that would be necessary for in situ, proxy measurements of particulate $Fe_{dith}$. Such measurements would be possible only under conditions of high UV particulate absorption, relative to total absorption, and in the absence of non-mineral UV absorption features with significant curvature, such as those linked to mycosporine-like amino acids. Under these conditions, a spectral curvature-based optical proxy (such as $\Delta a_{2d}(382)$ or $\Delta a_{2d}(435)$) for $Fe_{dith}$ would need to include high signal-to-noise, hyperspectral, UV absorption measurements coupled with a proxy for particle mass concentration (such as backscattering at a red wavelength). A location-specific calibration would be necessary to constrain the uncertainty stemming from variations in particle size distribution, aggregation state, CDOM, and phytoplankton absorption.

Particle mass-specific absorption properties are important parameters in optical and remote sensing models for coastal regions. The data set presented here confirms and quantifies the primary role of iron oxides in the UV and visible absorption properties of suspended mineral particles that are prevalent along turbid, river-dominated coastlines such as the northern Gulf of Mexico. Our measurements also suggest that OC content of suspended, mostly mineral particles plays a smaller and more variable role in particulate absorption in coastal Louisiana. While preliminary, data here suggest a relationship between mineral particle absorption at near-infrared wavelengths and non–dithionite-extractable iron content (which in this study may have included pyrite iron). At UV and blue wavelengths, changes in iron oxide–specific absorption features appear quantifiable for suspended riverine and coastal particles over their natural range of iron oxide contents. This possibility suggests the development of optical techniques allowing in situ observation of iron mineral transformations.

*Acknowledgments*

Mary Jane Perry provided lab space and equipment for optical analyses performed in this study. The comments of Dariusz Stramski and two anonymous reviewers contributed substantially to this paper. We would like to acknowledge funding support from the National Science Foundation Chemical Oceanography program (L.M. and M.L.E.), a National Aeronautics and Space Administration Earth Systems Science Graduate Fellowship (M.L.E.), and the Office of Naval Research Environmental Optics program (E.B. and C.R.).

## References

Allison, M., G. Kineke, E. Gordon, and M. Goni. 2000. Development and reworking of a seasonal flood deposit on the inner continental shelf of the Atchafalaya River. *Cont. Shelf Res.* **20:** 2267–2294, doi:10.1016/S0278-4343(00)00070-4

Babin, M., and D. Stramski. 2002. Light absorption by aquatic particles in the near-infrared spectral region. Limnol. Oceanogr. **47:** 911–915, doi:10.4319/lo.2002.47.3.0911

———, and ———. 2004. Variations in the mass-specific absorption coefficient of mineral particles suspended in water. Limnol. Oceanogr. **49:** 756–767, doi:10.4319/lo.2004.49.3.0756

———, ———, G. M. Ferrari, H. Claustre, A. Bricaud, G. Obolensky, and N. Hoepffner. 2003. Variations in the light absorption coefficients of phytoplankton, nonalgal particles, and dissolved organic matter in coastal waters around Europe. J. Geophys. Res. **108:** 3211, doi:10.1029/2001JC000882

Bélanger, S., M. Babin, and P. Larouche. 2008. An empirical ocean color algorithm for estimating the contribution of chromophoric dissolved organic matter to total light absorption in optically complex waters. J. Geophys. Res. **113:** C04027, doi:10.1029/2007JC004436

Bertsch, P. M., and P. R. Bloom. 1996. Aluminum, p. 639–664. *In* D. L. Sparks [ed.], Methods of soil analysis. Part 3: Chemical methods. Soil Science Society of America.

Bettiol, C., L. Stievano, M. Bertelle, F. Delfino, and E. Argese. 2008. Evaluation of microwave-assisted acid extraction procedures for the determination of metal content and potential bioavailability in sediments. Appl. Geochem. **23:** 1140–1151, doi:10.1016/j.apgeochem.2007.11.008

Bither, T. A., R. J. Bouchard, W. H. Cloud, P. C. Donohue, and W. J. Siemons. 1968. Transition metal pyrite dichalcogenides. High-pressure synthesis and correlation of properties. Inorg. Chem. **7:** 2208–2220, doi:10.1021/ic50069a008

Boss, E., W. Slade, and P. Hill. 2009. Effect of particulate aggregation in aquatic environments on the beam attenuation and its utility as a proxy for particulate mass. Opt. Express **17:** 9408–9420, doi:10.1364/OE.17.009408

Bowers, D. G., and C. E. Binding. 2006. The optical properties of mineral suspended particles: A review and synthesis. Estuar. Coast. Shelf Sci. **67:** 219–230, doi:10.1016/j.ecss.2005.11.010

Bricaud, A., and D. Stramski. 1990. Spectral absorption coefficients of living phytoplankton and nonalgal biogenous matter: A comparison between the Peru upwelling area and the Sargasso Sea. Limnol. Oceanogr. **35:** 562–582, doi:10.4319/lo.1990.35.3.0562

Canfield, D. E. 1989. Reactive iron in marine sediments. Geochim. Cosmochim. Acta **53:** 619–632, doi:10.1016/0016-7037(89)90005-7

Del Vecchio, R., and A. Subramaniam. 2004. Influence of the Amazon River on the surface optical properties of the western tropical North Atlantic Ocean. J. Geophys. Res. **109:** C11001, doi:10.1029/2004JC002503

Doxaran, D., K. Ruddick, D. McKee, B. Gentili, D. Tailliez, M. Chami, and M. Babin. 2009. Spectral variations of light scattering by marine particles in coastal waters, from the visible to the near infrared. Limnol. Oceanogr. **54:** 1257–1271, doi:10.4319/lo.2009.54.4.1257

D'Sa, E., R. Miller, and C. Del Castillo. 2006. Bio-optical properties and ocean color algorithms for coastal waters influenced by the Mississippi River during a cold front. Appl. Opt. **45:** 7410–7428, doi:10.1364/AO.45.007410

Duysens, L. N. M. 1956. The flattering of the absorption spectrum of suspensions, as compared to that of solutions. Biochim. Biophys. Acta **19:** 1–12, doi:10.1016/0006-3002(56)90380-8

Effler, S. W., M. Perkins, F. Peng, C. Strait, A. D. Weidemann, and M. T. Auer. 2011. Light-absorbing components in Lake Superior. J. Great Lakes Res. **36:** 656–665, doi:10.1016/j.jglr.2010.08.001

Egan, W. G., and T. W. Hilgeman. 1979. Optical properties of inhomogeneous materials: Applications to geology, astronomy, chemistry, and engineering, Academic Press.

Estapa, M. L., and L. M. Mayer. 2010. Photooxidation of particulate organic matter, carbon/oxygen stoichiometry, and related photoreactions. Mar. Chem. **122:** 138–147, doi:10.1016/j.marchem.2010.06.003

Ferrari, G. M., and S. Tassan. 1999. A method using chemical oxidation to remove light absorption by phytoplankton pigments. J. Phycol. **35:** 1090–1098, doi:10.1046/j.1529-8817.1999.3551090.x

Gleyzes, C., S. Tellier, and M. Astruc. 2002. Fractionation studies of trace elements in contaminated soils and sediments: A review of sequential extraction procedures. Trends Anal. Chem. **21:** 451–467, doi:10.1016/S0165-9936(02)00603-9

Horowitz, A. J., K. A. Elrick, and J. J. Smith. 2001. Annual suspended sediment and trace element fluxes in the Mississippi, Columbia, Colorado, and Rio Grande drainage basins. Hydrol. Process. **15:** 1169–1207, doi:10.1002/hyp.209

Johnson, A. G., and J. T. Kelley. 1984. Temporal, spatial, and textural variation in the mineralogy of Mississippi River suspended sediment. J. Sediment. Petrol. **54:** 67–72.

Khelifa, A., and P. S. Hill. 2006. Models for effective density and settling velocity of flocs. J. Hydraulic Res. **44:** 390–401, doi:10.1080/00221686.2006.9521690

Kineke, G. C., E. E. Higgins, K. Hart, and D. Velasco. 2006. Fine-sediment transport associated with cold-front passages on the shallow shelf, Gulf of Mexico. Cont. Shelf Res. **26:** 2073–2091, doi:10.1016/j.csr.2006.07.023

Kishino, M., M. Takahashi, N. Okami, and S. Ichimura. 1985. Estimation of the spectral absorption coefficients of phytoplankton in the sea. Bull. Mar. Sci. **37:** 632–642.

Kosmas, C. S., N. Curi, R. B. Bryant, and D. P. Franzmeier. 1984. Characterization of iron oxide minerals by second-derivative visible spectroscopy. Soil Sci. Soc. Am. J. **48:** 401–405, doi:10.2136/sssaj1984.03615995004800020036x

Link, D. D., P. J. Walter, and H. M. Kingston. 1998. Development and validation of the new EPA microwave-assisted leach method 3051A. Environ. Sci. Technol. **32:** 3628–3632, doi:10.1021/es980559n

Loeppert, R. H., and W. P. Inskeep. 1996. Iron, p. 639–664. *In* D. L. Sparks [ed.], Methods of soil analysis. Part 3: Chemical methods. Soil Science Society of America.

Mayer, L. M. 1982. Aggregation of colloidal iron during estuarine mixing: Kinetics, mechanism, and seasonality. Geochim. Cosmochim. Acta **46:** 2527–2535, doi:10.1016/0016-7037(82)90375-1

———. 1994. Surface area control of organic carbon accumulation in continental shelf sediments. Geochim. Cosmochim. Acta **58:** 1271–1284, doi:10.1016/0016-7037(94)90381-6

———, L. L. Schick, K. Skorko, and E. Boss. 2006. Photodissolution of particulate organic matter from sediments. Limnol. Oceanogr. **51:** 1064–1071, doi:10.4319/lo.2006.51.2.1064

Meier, L. P., and A. P. Menegatti. 1997. A new, efficient, one-step method for the removal of organic matter from clay-containing sediments. Clay Miner. **32:** 557–563, doi:10.1180/claymin.1997.032.4.06

Mitchelson, E. G., N. J. Jacob, and J. H. Simpson. 1986. Ocean colour algorithms for case 2 waters of the Irish sea in comparison to algorithms from case 1 waters. Cont. Shelf Res. **5:** 403–415, doi:10.1016/0278-4343(86)90005-1

Nelson, J. R., and C. Y. Robertson. 1993. Detrital spectral absorption: Laboratory studies of visible light effects on phytodetritus absorption, bacterial spectral signal, and comparison to field measurements. J. Mar. Res. **51:** 181–207, doi:10.1357/0022240933223864

Poulton, S. W., and R. Raiswell. 2002. The low-temperature geochemical cycle of iron: From continental fluxes to marine sediment deposition. Am. J. Sci. **302:** 774–805, doi:10.2475/ajs.302.9.774

———, and ———. 2005. Chemical and physical characteristics of iron oxides in riverine and glacial meltwater sediments. Chem. Geol. **218:** 203–221, doi:10.1016/j.chemgeo.2005.01.007

Raiswell, R., D. E. Canfield, and R. A. Berner. 1994. A comparison of iron extraction methods for the determination of degree of pyritisation and the recognition of iron-limited pyrite formation. Chem. Geol. **111:** 101–110, doi:10.1016/0009-2541(94)90084-1

Schaeffer, B. A., R. N. Conmy, J. Aukamp, G. Craven, and E. J. Ferer. 2011. Organic and inorganic matter in Louisiana coastal waters: Vermilion, Atchafalaya, Terrebonne, Barataria, and Mississippi regions. Mar. Pollut. Bull. **62:** 415–422, doi:10.1016/j.marpolbul.2010.12.004

Schwertmann, U., and R. M. Cornell. 1991. Iron oxides in the laboratory: Preparation and characterization. VCH Publishers.

Sherman, D., and T. Waite. 1985. Electronic spectra of $Fe^{3+}$ oxides and oxide hydroxides in the near IR to near UV. Am. Mineral. **70:** 1262–1269.

Snyder, W. A., and others. 2008. Optical scattering and backscattering by organic and inorganic particulates in US coastal waters. Appl. Opt. **47:** 666–677, doi:10.1364/AO.47.000666

Son, Y. B., W. D. Gardner, A. V. Mishonov, and M. J. Richardson. 2009. Multispectral remote-sensing algorithms for particulate organic carbon (POC): The Gulf of Mexico. Remote Sens. Environ. **113:** 50–61, doi:10.1016/j.rse.2008.08.011

Southwell, M., R. Kieber, R. Mead, G. Brooks Avery, and S. Skrabal. 2010. Effects of sunlight on the production of dissolved organic and inorganic nutrients from resuspended sediments. Biogeochemistry **98:** 115–126, doi:10.1007/s10533-009-9380-2

Stramski, D. 1990. Artifacts in measuring absorption spectra of phytoplankton collected on a filter. Limnol. Oceanogr. **35:** 1804–1809, doi:10.4319/lo.1990.35.8.1804

———, M. Babin, and S. Woźniak. 2007. Variations in the optical properties of terrigenous mineral-rich particulate matter suspended in seawater. Limnol. Oceanogr. **52:** 2418–2433, doi:10.4319/lo.2007.52.6.2418

Stucki, J. W., and P. R. Lear. 1989. Variable oxidation states of iron in the crystal structure of smectite clay minerals, *In* L. M. Coyne, S. W. S. McKeever, and D. F. Blake [eds.], Spectroscopic characterization of minerals and their surfaces. American Chemical Society.

Tessier, A., P. G. C. Campbell, and M. Bisson. 1979. Sequential extraction procedure for the speciation of particulate trace metals. Anal. Chem. **51:** 844–851, doi:10.1021/ac50043a017

Trefry, J. H., and B. J. Presley. 1982. Manganese fluxes from Mississippi Delta sediments. Geochim. Cosmochim. Acta **46:** 1715–1726, doi:10.1016/0016-7037(82)90112-0

van de Hulst, H. C. 1957. Light scattering by small particles. John Wiley and Sons.

Wagai, R., and L. M. Mayer. 2007. Sorptive stabilization of organic matter in soils by hydrous iron oxides. Geochim. Cosmochim. Acta **71:** 25–35, doi:10.1016/j.gca.2006.08.047

Werdell, P. J., and C. S. Roesler. 2003. Remote assessment of benthic substrate composition in shallow waters using multispectral reflectance. Limnol. Oceanogr. **48:** 557–567, doi:10.4319/lo.2003.48.1_part_2.0557

Woźniak, S. B., and others. 2010. Optical variability of seawater in relation to particle concentration, composition, and size distribution in the nearshore marine environment at Imperial Beach, California. J. Geophys. Res. **115:** C08027, doi:10.1029/2009JC005554

*Associate editor: Dariusz Stramski*

*Received: 15 January 2011*
*Accepted: 15 September 2011*
*Amended: 22 September 2011*